

Profiles of spectral lines from failed and decelerated winds from neutron stars and black holes

A. V. Dorodnitsyn[★]

Laboratory for High Energy Astrophysics, NASA Goddard Space Flight Center, Code 662, Greenbelt, MD 20771, USA

Accepted 2010 March 22. Received 2010 March 22; in original form 2009 December 5

ABSTRACT

We calculate profiles of spectral lines from an extended outflow from the compact object (a black hole or a neutron star). We assume that the bulk velocity of the flow increases during a short phase of acceleration and then rapidly decreases forming a failed wind. We also study the wind which is only decelerating. We show that depending on the relative strength of the gravitational redshifting line profiles from such winds may be of several types: distorted P-Cygni (emission and blueshifted absorption); W-shaped (absorption–emission–absorption) and inverted P-Cygni (emission–redshifted absorption). The latter case is expected from accretion flows where the velocity is directed inwards; however, we show that inverted P-Cygni profile can be produced by the failed wind, provided the line is formed within several tens of Schwarzschild radii from the compact object.

Key words: line: formation – radiation mechanisms: general – radiative transfer – stars: mass-loss – stars: winds, outflows – galaxies: active.

1 INTRODUCTION

Relativistically broadened, double horn profiles from fluorescent Fe $K\alpha$ lines is a widely accepted evidence for the presence of the cold accretion disc in type 1 Seyfert (Seyfert 1) active galactic nuclei (AGN) and the assumption that such disc is illuminated by X-rays generated by the corona (see e.g. Fabian et al. 2000). However, the geometrically broad line forming region spans a large range of orbital velocities which translates to a broad region in frequency space, additionally skewing the line by relativistic effects and making detailed diagnostics of the accreting plasma difficult.

Spectral resolution of grating spectrographs of the X-ray telescopes *Chandra* and *XMM-Newton* below ~ 10 keV allows observations revealing complicated structure of the $K\alpha$ line, in many type 1 AGN (e.g. Reeves et al. 2001) and for the detection of the narrow core see also Yaqoob & Padmanabhan (2003). Observations suggest that distant parts of the accretion disc as well as the reflection from the obscuring torus are involved. Multidimensional simulations of spectra of warm absorber flows by Dorodnitsyn & Kallman (2009) also show the importance of distant AGN winds for the formation of the complex structure of Fe $K\alpha$ line.

It is widely accepted that strong gravitational field of the compact object, such as black hole (BH) or neutron star (NS) can imprint itself into the radiation which comes from regions within several tens of Schwarzschild radii, r_g . Narrow emission and absorption

lines from BHs and NSs deliver an optimal opportunity to deduce their masses and radii (in case of NS).

Narrow lines formed near a BH carry direct information about the dynamics, ionization stage and covering fraction of the absorbing gas and thus about the mass budget of the inflow/outflow. The latter is important for understanding of the fraction of the AGN–host galaxy feedback which comes directly from regions close the BH. Gravitational redshifting is entangled with Doppler shifts, and altogether they encode information about the mass of the BH.

Observed narrow absorption features from several Quasars and Seyfert galaxies possibly reveal the importance of gravitational redshifting and Doppler blueshifting and redshifting due to the bulk motion of the moving gas. Such evidence was found in several cases including: Seyfert 1 galaxy NGC 3516 where it is suggested that observed absorption features are from the gravitationally redshifted resonant line scattering within the accretion flow (Nandra et al. 1999); the gravitationally redshifted (10–20 r_g from the BH) resonance absorption line from Fe xxv or Fe xxvi in the quasar E1821+643 (Yaqoob & Serlemitsos 2005); a combination of the gravitational and Doppler shifting of lines from ionized iron is suggested to explain absorption features from the quasar PG 1211+143 by Reeves et al. (2005), also see Matt et al. 2005 for possible detection of the strongly redshifted, transient absorption feature from ionized Fe in the quasar Q0056–363).

Dadina et al. (2005) reported on the redshifted absorption, and emission features observed at ~ 6 keV, from Seyfert 1 galaxy Mrk 509. Two of the absorption features are separated by the emission line, and the overall emission structure is attributed to H- or He-like iron. This W-shaped structure is found to be sporadic with

[★]E-mail: dora@milkyway.gsfc.nasa.gov

variability as short as ~ 20 ks. Infall and outflow, $\sim \pm (0.1-0.2)c$, of matter are suggested, together with the gravitational redshifting to explain these features. Transient nature of such features is consistent with the latter non-detection of the redshifted absorption and the detection of only blueshifted absorption lines (Capri et al. 2009).

The detection of the redshifted absorption lines from accreting NSs which exhibit thermonuclear X-ray bursts are ideally suited for deducing the NS mass and putting constraints on its equation of state. So far, these detections are rare. Cottam, Paerels & Mendez (2002) identified several absorption features in the burst spectra of the NS EXO 0748–676. Lines from H-like iron for the early phases of the burst and He-like iron for the late phases were adopted to explain the spectra and to obtain the redshift of $Z = 0.35$. Other studies including LTE and non-LTE NS atmosphere modelling suggested $n = 2-3$ transition of Fe xxiv and the redshift $Z = 0.24$ (Rauch, Suleimanov & Werner 2008). These lines are expected to be intrinsically transient which additionally lowers the statistical significance of such detections.

Usually, the existing models of gravitationally redshifted lines do not include influence of the transfer effects in the extended moving envelope, and if they do simple transmission models are adopted. Large intensities of emission components and simultaneous presence of emission and absorption from the same line transition suggest the importance of the coupling between dynamics of the wind and gravitational redshifting.

Beginning from works of Beals (1931), it was understood that P-Cygni profiles provide a unique evidence for the rapidly moving wind. It was also understood that radiation from a huge volume occupied by such wind naturally explains bright emission features in the spectra, and the observed broadening is due to high-velocity dispersion of such wind (few $\times 10^3$ km s $^{-1}$ in the case of a normal star). The most remarkable about this profile is, of course, the relative blueshifting of the absorption trough relative to the emission line. As a P-Cygni profile bears an imprint of the bulk motion of the plasma, it is an important tool of the diagnostics of the dynamics of stellar winds.

In the paper by Dorodnitsyn (2009, hereafter Paper I), a modified Sobolev approximation was built which incorporates gravitational redshifting, and spectral line profiles were calculated from a stellar-type and explosion-type winds, accelerated in the strong gravitational field of the compact object.

An important parameter from Paper I measures the relative importance of gravity at the wind base $g_0 = R_c/r_g$, where R_c is the radius of the wind launching point. Two types of the velocity laws were adopted: (i) ‘stellar’ type, i.e. $v(r) \sim (1 - R_c/r)^m$, and (ii) homologous expansion $v(r) \sim r$ (Hubble law), adopted for the description of outbursts. Important also found the terminal velocity, V^∞ , which spans a range of $0.01-0.3c$ and the distribution of the opacity.

It was found that gradually accelerated winds which are launched at $R_c \lesssim 20-30 r_g$ produce the following types of profiles: (i) distorted P-Cygni, i.e. characterized by emission feature which is redshifted relative to an absorption trough; (ii) sawtooth, i.e. the narrow redshifted absorption line superimposed on a broader redshifted emission line, combined additionally with a blueshifted absorption line and (iii) W-shaped, i.e. absorption–emission–absorption, profiles (by ‘redshifted’ or ‘blueshifted’ we necessarily mean only the relative blueshift, redshift of one spectral feature with respect to the other, which may or may not represent the actual shift of frequency of such feature with respect to the rest frequency of the line).

In this paper, we calculate profiles of lines from a wind which is either everywhere decelerated, i.e. described by the $v \sim 1/r^m$ law,

or failed, i.e. its velocity rises steeply during the short acceleration phase and then decreases, asymptotically approaching $v \sim 1/r^m$ law.

We will show that line profiles from failed winds are significantly different from those considered in Paper I. Additionally to three types described above there is a fourth type: the inverted P-Cygni profile (absorption–emission). Note that the inverted P-Cygni profile is expected from spherically symmetric accretion flow, and to observe it from the wind is counterintuitive. We will show that strong gravitational redshifting together with the ‘failed’ character of the wind and also provided the deceleration phase is fast (i.e. $m \gtrsim 3$) are necessary conditions for the appearance of this feature. Failed wind profiles can also be W shaped or sawtooth shaped.

The plan of this paper is as follows: in Section 2, we review basic assumptions of Paper I about the wind geometry and gravitational field; in Section 3, we describe our methods of calculation of line profiles i.e. the Sobolev optical depth of the line, source functions, calculate mean radiation field etc.; in Section 4, we describe velocity laws, derive the bridging formula for the failed wind and make assumptions about the distribution of the opacity; in Section 5, we calculate equal frequency surfaces, which are of paramount importance to understand line profiles which we calculate in Section 6; in Sections 7 and 8, we discuss major results and conclude.

2 ASSUMPTIONS AND APPROXIMATIONS

We assume that photons from an external source of continuum radiation are interacting with the wind via resonance line scattering, both the wind and the radiation source are assumed to be spherically symmetric, the wind is launched from the photosphere of the radius R_c , there is a prescribed velocity profile, $v(r)$, and a prescribed distribution of the line opacity in the wind. The only difference in the assumptions from those of Paper I is that here we consider decelerating winds, instead of winds which are gradually increasing their velocity. Profiles from decelerated winds from normal stars were calculated in works of different authors (e.g. Kuan & Kuhl 1975; Marti & Noerdlinger 1977). In the following, we briefly summarize the formalism developed in Paper I.

We assume that after leaving the photosphere a photon is travelling in the wind without interaction with the matter except for certain points (resonances) where it is frequency in the comoving frame, $\tilde{\nu}$ appears to be within the Doppler thermal width of the spectral line, $\Delta\nu_D = \nu_0 v_{th}/c$, where v_{th} is the thermal velocity, and ν_0 is the frequency at the line centre. To allow for the resonance region to be located as close as several Schwarzschild radii, $r_g = 2GM/c^2$, from the compact object we take into account both Doppler and gravitational shifting of the photon’s frequency. The Lorentz transformations from a local Lorentzian frame (a photon frequency ν_{loc}) which is at rest at a given point s_0 to the comoving frame give $\tilde{\nu} = \gamma \nu_{loc} (1 - \mu\beta)$, where $\beta \equiv v/c$, $\gamma \equiv (1 - \beta^2)^{-1/2}$. A photon that was emitted at the point s_0 after travelling to some other point s is gravitationally redshifted and blueshifted and in the comoving frame has the following frequency: $\tilde{\nu}(s) = \gamma \nu_{loc}(s_0) \sqrt{g_{00}(s_0)/g_{00}(s)} [1 - \mu(s)\beta(s)]$.

Gravitational field is described in a ‘weak-field limit’, i.e. by means of the gravitational potential, ϕ , and also implying $\sqrt{g_{00}} \simeq 1 + \phi/c^2$. To allow for the terminal velocity, V^∞ , to be of the order of the escape velocity V_{esc} at the base of the wind (which can be a large fraction of the speed of light, c), we must retain all terms of the order of v^2/c^2 and ϕ/c^2 .

The photon emitted at the point s , in a direction \mathbf{n} , having the frequency $\tilde{\nu}$ will be registered by the observer at infinity at the

frequency ν^∞ :

$$\tilde{\nu}(s) = \nu^\infty \left[1 - \mu(s)\beta(s) - \frac{\phi(s)}{c^2} + \frac{\beta(s)^2}{2} \right], \quad (1)$$

where $\mu = \mathbf{n} \cdot \mathbf{v} = \cos \theta$ and ϕ is the gravitational potential.

It is convenient to adopt dimensionless units: the non-dimensional frequency, $y = (\nu - \nu_0)/\Delta\nu_D$; the non-dimensional radius, $x = r/R_c$; the non-dimensional velocity, $u = v/v_{th}$, and the non-dimensional gravitational potential $\Phi = \phi/(c v_{th}) = \zeta(\phi/c^2)$, where $\zeta = c/v_{th}$. In the narrow-line limit, the emitted frequency is ν_0 and thus

$$y^\infty = (\nu^\infty - \nu_0)/\Delta\nu_D. \quad (2)$$

In such non-dimensional units, the equation (1) can be cast in the form

$$y^\infty = \mu u(x) + \Phi(x) - u(x)^2/(2\zeta). \quad (3)$$

Equation (3) determines the position of the resonant point. It is straightforward to rewrite the above equations in terms of the redshift, $Z = (\tilde{\nu} - \nu^\infty)/\nu^\infty$:

$$y^\infty = -\zeta \frac{Z}{1+Z}, \quad (4)$$

and from equation (3) we obtain

$$Z = -\frac{\mu u + \Phi - u^2/(2\zeta)}{\zeta + \mu u + \Phi - u^2/(2\zeta)}. \quad (5)$$

To describe gravitational field, we adopt two types of potentials: the Newtonian potential, $\phi(r) = -\frac{GM}{r}$, and the pseudo-Newtonian potential of Paczynski–Wiita (PW; Paczynski & Wiita 1980):

$$\phi(r) = \frac{GM}{r_g - r}. \quad (6)$$

The latter mimics important features of exact general relativistic solutions for particle trajectories near a Schwarzschild BH. For example, it reproduces the positions of both the last stable circular orbit, located at $3r_g$ and the marginally bound circular orbit at $2r_g$. The non-dimensional form of the PW potential (6) reads: $\Phi(x) = \zeta/[2(1 - xg_0)]$. A non-dimensional parameter, $g_0 = R_c/r_g$, determines the relative importance of the gravitational redshifting (i.e. by equating $g_0 \rightarrow \infty$ one completely neglects the influence of the gravitational field on the energy of a photon).

We adopt a (p, z) coordinate system, such that $x = \sqrt{p^2 + z^2}$, where p is the impact parameter and the observer is located at $z = \infty$. In the non-dimensional variables, equation (3) takes the form

$$y^\infty = \frac{z_0}{\sqrt{z_0^2 + p^2}} u \left(\sqrt{z_0^2 + p^2} \right) + \Phi \left(\sqrt{z_0^2 + p^2} \right) - \frac{1}{2\zeta} u^2 \left(\sqrt{z_0^2 + p^2} \right). \quad (7)$$

The solution of the equation (7) for different values of p determines the locus and shape of the equal-frequency surface (EFS). Understanding the shape and topology of EFS is very helpful in order to understand and interpret profiles of spectral lines from the moving medium. Note that equation (7) does not reference to any particular form of the velocity law, $v(r)$. In the absence of gravitational redshifting, the first term on the right-hand side of (7) determines the locus of the surfaces of equal line-of-sight velocities. The second and third terms stand for the gravitational redshifting and transverse Doppler effect (also redshifting). Equation (7) was derived in Paper I, where its properties are investigated for the case of the outwardly accelerated wind. Here, we study this equation from the perspective of decelerated winds.

3 CALCULATION OF LINE PROFILES: METHODS

Including gravitational redshifting into the frame of the Sobolev approximation requires to take into account terms of the order of $\mathcal{O}(v^2/c^2)$. Sobolev optical depth enters Castor's (Castor 1970) escape probabilities, thus not only making them dependent on $d\phi/ds$ but also demanding to include $\mathcal{O}(v^2/c^2)$ terms into their derivation. A Sobolev approximation (e.g. Sobolev 1960; Rybicki & Hummer 1978) which takes into account all of the above assumptions was developed in Paper I, and including decelerating wind into consideration leaves this formalism intact. The Sobolev length, L_{sob} , is defined as a characteristic length over which the photon propagating in the direction s stays in resonance with a certain line transition: $L_{sob} \simeq v_{th}/|dv/ds + (1/c)d\phi/ds|$. The optical thickness in the direction s is

$$\tau_{sob} = \chi_{0,com}^l \times L_{sob}. \quad (8)$$

The Sobolev optical depth in a line is found from the relation

$$\tau_l = \chi_{0,com}^l \frac{r}{\beta} \left[1 + \beta^2(1 + \mu^2) - 2\mu\beta - \frac{\phi}{c^2} \right] \left[1 - \mu^2 \left(1 - \frac{d \ln \beta}{d \ln r} \right) + \mu \left(\frac{1}{\beta c^2} \frac{d\phi}{d \ln r} - \beta \frac{d \ln \beta}{d \ln r} \right) \right]^{-1}, \quad (9)$$

where $\chi_{0,com}^l$ is the opacity at the line frequency in the comoving frame:

$$\chi_{0,com}^l = \frac{\pi e^2}{mc} (gf) \frac{N_l/g_l - N_u/g_u}{\Delta\nu}, \quad (10)$$

where N_u, N_l and g_u, g_l are populations and statistical weights of the corresponding levels of the transition and f is the oscillator strength of the transition. Retaining terms of the order of $\mathcal{O}(v^2/c^2)$, we recast equation (9) in the form

$$\tau_l = \tau_r \times \left\{ \frac{d \ln \beta}{d \ln r} [1 + \beta(1 - 2\mu)] + \frac{1}{c^2 \beta} \frac{d\phi}{d \ln r} \right\} \times \left[1 - \mu^2 \left(1 - \frac{d \ln \beta}{d \ln r} \right) + \mu \left(\frac{1}{\beta c^2} \frac{d\phi}{d \ln r} - \beta \frac{d \ln \beta}{d \ln r} \right) \right]^{-1}, \quad (11)$$

where $\tau_r = \tau_l(\mu = 1)$ is the optical depth in the radial direction. The Sobolev approximation consists of two parts: (i) calculation of the optical depth of a resonant layer (i.e. from 9) and (ii) calculation of the source function S_ν . Considering the scattering within a line and adopting complete frequency redistribution and isotropic scattering matrix, the source function can be approximated as (i.e. Hummer 1969)

$$S_\nu \simeq (1 - \epsilon) J_\nu + \epsilon B_\nu, \quad (12)$$

where J_ν is the mean intensity and B_ν is the Planck function. ϵ is the ratio of collisional and de-excitation rates.

In order to calculate the source function and then, finally, the emergent intensity, we adopt a method of escape probabilities of Castor (1970). In this approach, the mean intensity J_ν is found from averaging of the formal solution of the radiation transfer equation over all solid angles; the result is

$$J_\nu = S_\nu(1 - P_{esc}) + J_{dist}(P_{pen}), \quad (13)$$

where P_{esc} is the probability for a photon to escape from the resonant region, J_{dist} is the contribution to the mean radiation field delivered by the distant core and P_{pen} is the probability for a photon, which is issued by the core, to penetrate to the given point. Combining (12)

and (13) in a single linear equation and solving for S_v , we obtain $S_v \sim J_{\text{dist}}(P_{\text{pen}})/P_{\text{esc}}$ (note that we assumed $\epsilon = 0$). The probability for a photon to escape in a direction μ reads:

$$P_{\text{esc}} = \langle P_{\text{loc}}^\mu (1 + \beta^2(3\mu^2 - 1) + 2\mu\beta) \rangle, \quad (14)$$

where $\langle \rangle$ denotes angular averaging: $\langle f \rangle_\Omega = \frac{1}{4\pi} \int_\Omega f(\Omega') d\Omega'$, and P_{loc}^μ is the non-relativistic expression for the directional escape probability:

$$P_{\text{loc}}^\mu = \frac{1 - \exp[-\tau_1(\mu, s)]}{\tau_1(s, \mu)}, \quad (15)$$

where τ_1 is obtained from (9). We assume that the core emits continuum blackbody radiation, with no limb darkening, and that in the vicinity of the line the continuum may be approximated as constant. Integrating P_{loc}^μ over the maximum angle subtended by the core: $\theta_c = \arccos \mu_c = \arccos \sqrt{1 - x^{-2}}$, the probability for a photon to penetrate to a given point reads:

$$P_{\text{pen}} = \langle P_{\text{loc}}^\mu \rangle_{4\pi W}, \quad (16)$$

where W is a dilution factor:

$$W = \frac{1}{2} (1 - \mu_c). \quad (17)$$

The distant contribution, J_{dist} , is calculated from

$$J_{\text{dist}} = I_c P_{\text{pen}} \quad (18)$$

and for the source function, S_v , we have

$$S_v = \frac{J_v}{P_{\text{esc}}} [1 + \beta^2(3\mu^2 - 1) + 2\mu\beta]. \quad (19)$$

In the presence of non-monotonic velocity law, for example when the wind first accelerates and then decelerates, multiple resonances may occur. This is best studied adopting a concept of EFSs (see the next section). At the i th resonance, the radiation field suffers a change: some photons from directions other than that of the ray are scattered into the direction of the observer (local contribution); the other contribution is due to the incident intensity which is attenuated at this point:

$$I_{\text{res}} = I_{\text{inc}} e^{-\tau_{1,i}} + S_i (1 - e^{-\tau_{1,i}}), \quad (20)$$

where S_i is the source function at the i th resonance. The source function S_i is anisotropic in the direction of motion and was calculated in the relativistic case in the paper by Hutsemekers & Surdej (1990). Note that these authors calculated the full relativistic source function and our calculations take into account the contribution from the gravitation shifting and also from the relativistic effects which are included by retaining $\mathcal{O}(v^2/c^2)$ terms.

We assume that resonant interaction of photons and matter takes place while propagating only in the forward direction (in the direction towards the observer) and that all other possible interactions are neglected. Altogether, these assumptions are known as the disconnected approximation (Grachev & Grinin 1975; Marti & Noerdlinger 1977; Rybicki & Hummer 1978, 1983). It is usually adopted in the multiple resonance case (see Paper I for the discussion of approximations).

Our computational domain has a spherical shape of a radius p_{out} . A ray with impact parameter p intersects this sphere in two places: z_1 and $z_2 > z_1$. To obtain the emergent intensity, we sum the expression (20) over all resonances along the ray with impact parameter p . The total number of resonances is not known a priori and thus the procedure of the calculation of the total intensity is best cast in the form of a simple recurrence formula:

$$I_i(v^\infty, p) = I_{i-1} e^{-\tau_{1,i}} + S_i (1 - e^{-\tau_{1,i}}), \quad (21)$$

where $i = 1 \dots N$ and N is the total number of resonances, the initial intensity I_1 reads:

$$I_1 = \begin{cases} I_c, & p < R_c \\ S_0(1 - e^{-\tau_{1,0}}), & \end{cases} \quad (22)$$

where the subscript 0 refers to the point which is the farthest point along the ray from the observer in the computational domain i.e. closest to z_1 . Note that (21) being the summation formula, it accounts for the fact that we do not know the total number of resonances before we transfer a photon through the computational domain. Thus, we propagate the photon along its trajectory (i.e. along a straight line with impact parameter p and checking for the resonance with the line). At the i th resonance, we calculate I_i and go further; if another resonance is detected, this previous I_i becomes an I_{i-1} in a new iteration. Integration along the photon's trajectory is performed until the point z_2 is reached. All other couplings between resonances are neglected. Non-local coupling between resonances in the case of a normal hot-star, non-monotonic wind was investigated in Puls, Owocki & Fullerton (1993). From their results, we may expect our approximation of the photon transfer is accurate within 10 per cent.

After being normalized to the continuum flux, F_c , the radiation flux seen by the observer is calculated from the following:

$$F(v^\infty, p)/F_c = \int_0^\infty I^\infty(v^\infty, p) p dp, \quad (23)$$

where $I^\infty = I_N(v^\infty, p)$.

4 DISTRIBUTIONS OF THE VELOCITY AND OPACITY

In this paper, we consider two types of the velocity laws. Both are used to approximate a wind which failed to escape from the potential well. The first adopted law describes the decelerating wind,

$$u(x) = U^\infty \frac{1}{x^m}, \quad (24)$$

where $m > 0$ and $U^\infty = V^\infty/v_{\text{th}}$, V^∞ is a terminal velocity. Equation (24) describes the wind, decelerating from $r = R_c$ where its velocity has a maximum. A different approximation is used to describe the wind which is accelerating at the beginning but after reaching maximum velocity is decelerating:

$$u(x) = U_0 \left[\frac{1}{x^m} - (1 - w_0/U_0) e^{-(x-1)^m/\epsilon} \right], \quad (25)$$

where $w_0 = v(R_c)/V^\infty = 0.01$ and $0 < \epsilon < 0.1$ is related to the location or 'thickness' of the boundary layer, which allows a smooth matching of the inner, increasing solution with the outer, decreasing one. The value of U_0 is related to U^∞ and is calculated numerically so that $\max[u(x)] = U^\infty$. In the acceleration part, in the limit $\delta x = x - 1 \sim 0$, equation (25) reduces to $u(x) \sim \text{constant} \times (\delta x)^m + w_0$ and at infinity $1/x^m$ term in the equation (25) is the dominant one. Velocity profiles (24) and (25) are shown in Fig. 1 (left-hand panel) for different values of (m, ϵ) . In Paper I, explosion-type outbursts (described by the homologous, Hubble-type velocity law) and winds with a stellar-type velocity profile were considered. With simplifications already adopted in this paper, one can argue that there is no need in any further specification of the particular physical mechanism which could have lead to velocity laws (24) or (25) (although see discussion in Paper I). Having said that we consider them as a mere parameterization which may be relevant to the real failed or decelerated winds.

The distribution of the opacity is adopted from Castor & Lamers (1979), who made use of the fact that in the optically thin case

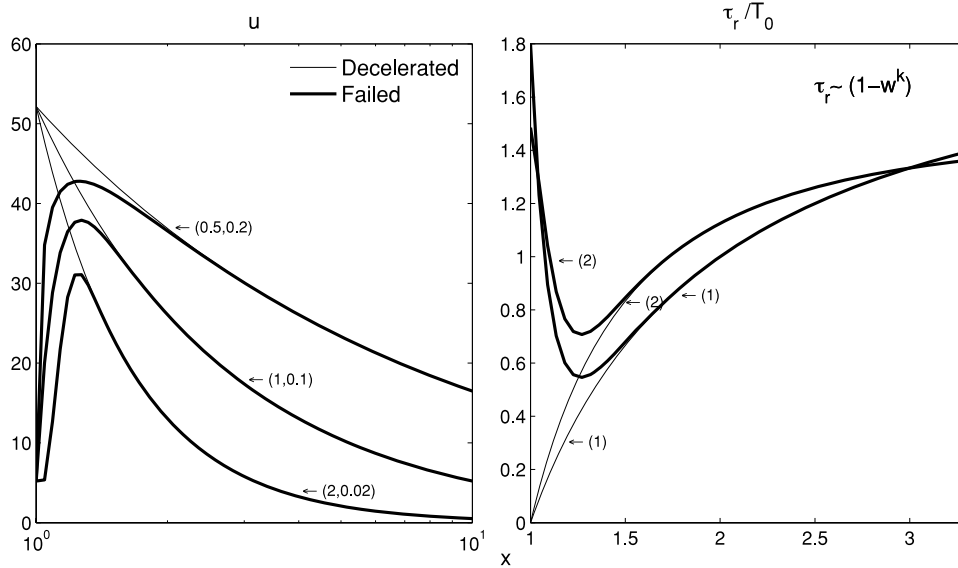


Figure 1. Velocity (left-hand panel) and opacity (right-hand panel) laws. Velocity curves: thin solid line (equation 24); thick solid line: (equation 25). Curves are labelled by pairs of m, ϵ . Opacity curves calculated from the equation (26) for corresponding velocity profiles; thin solid line – using equation (24) and thick solid line – using equation (25). Curves are marked by pairs of parameters p and ϵ from equation (26).

and the photoionization by diluted stellar continuum the ionization ratio of the successive stages is proportional to W/n , where W is the dilution factor and n is the number density. With the help of the continuity equation, in a spherically symmetric geometry, this ratio is proportional to v . It results in the parameterization of the radial optical depth $\tau_r = \tau_l(\mu = 1)$ in terms of the non-dimensional velocity, $w \equiv v/V^\infty$, and is written in the following form: $\tau_r \sim w$. Castor & Lamers (1979) also argued that $\tau_r \sim 1 - w$ law is somewhat more appropriate as the resultant P-Cygni profiles are closer to the observed ones. Note that in the absence of self-consistent modelling of the opacity distribution together with the dynamics of the flow any such profiling of the opacity should be considered with caution. Most important for our means is whether τ_r peaks close to the photosphere or at large radii. We chose the following parameterization of τ_r :

$$\tau_r(w) = T_0 \frac{k+1}{k} (1 - w^k), \quad (26)$$

where the parameter $k \geq 0$ and the parameter T_0 are related to the total optical depth at the line centre, $\int_0^1 \tau_r dw = T_0$. Fig. 1 (right-hand panel) shows distributions of the opacity (26) calculated from velocity laws (24) and (25) for different pairs of (m, ϵ) and for $k = 1$ and 2.

5 SURFACES OF EQUAL FREQUENCIES

Equation (3) determines the locus of EFS. That is, for a particular choice of the impact parameter, p and the frequency y^∞ , this equation determines the position of the resonant point, z_0 . In Paper I, it was shown that in strong gravitational field EFSs have complicated shape and topology. Those of them which are calculated for the redshifted photons may have branches situated between the star and observer. Of course, in the case of a normal stellar wind, photons which are emitted in the gas which is approaching the observer are blueshifted in the observer frame.

In the language of resonant surfaces, it means there are no redshifted EFS in front of the star [we call redshifted or blueshifted

EFS(v^∞) depending on whether v^∞ is blueshifted or redshifted]. If gravitational redshifting overwhelms Doppler boosting then in the observer frame these photons are redshifted.

It is useful to imagine resonant surfaces as partially transparent screens, which can scatter photons of a certain frequency. If EFS is situated in front of the star, it produces an absorption line according to $I_0 e^{-\tau_l}$, where I_0 is the incident intensity and τ_l is the line optical depth, otherwise EFS is reflecting, i.e. $I = (1 - e^{-\tau_l}) S$, where S is the source function. Note that EFS also can be multibranched.

The topology and shape of resonant surfaces in the case of the decelerated wind are different from those found in Paper I for the case of monotonically accelerated wind. In Paper I, it was found that sufficiently strong gravitational redshift can overwhelm Doppler blueshift which results in a redshifted EFS positioned in front of the star.

To calculate resonant surfaces, we introduce the following non-dimensional parameters: $\Lambda = y^\infty/y_{\max}^\infty = y^\infty/u_{\max}$, where $u_{\max} = U^\infty$ in the case of the velocity law (24) or the maximum velocity calculated from the velocity law (25) and the additional parameter $\beta_{\max} = (u_{\max}/c)v_{\text{th}}$. Rewriting equation (7), we obtain

$$\Lambda = \mu w(x) + \frac{1}{2(1 - xg_0)} \frac{1}{\beta_{\max}} - w(x)^2 \beta_{\max}. \quad (27)$$

Equation (27) is equivalent to equation (1). Note that if no relativistic corrections are taken into account (i.e. no last term on the right-hand side), and additionally the Newtonian potential is assumed the second term on the right-hand side becomes $-1/(2g_0 \beta_{\max}) x^{-1} = \text{constant} \times x^{-1}$ and the problem is described in terms of only two parameters.

EFSs calculated for the velocity law (24) are shown in Fig. 2. Upper-left plot shows EFS from the decelerated wind from the normal star, and its shape is well known (e.g. Kuan & Kuhi 1975; Marti & Noerdlinger 1977).

Increasing gravitational redshift significantly changes the shape and position of EFSs, advancing the redshifted EFS in front of the star and leading to formation of the redshifted absorption line or absorption edge.

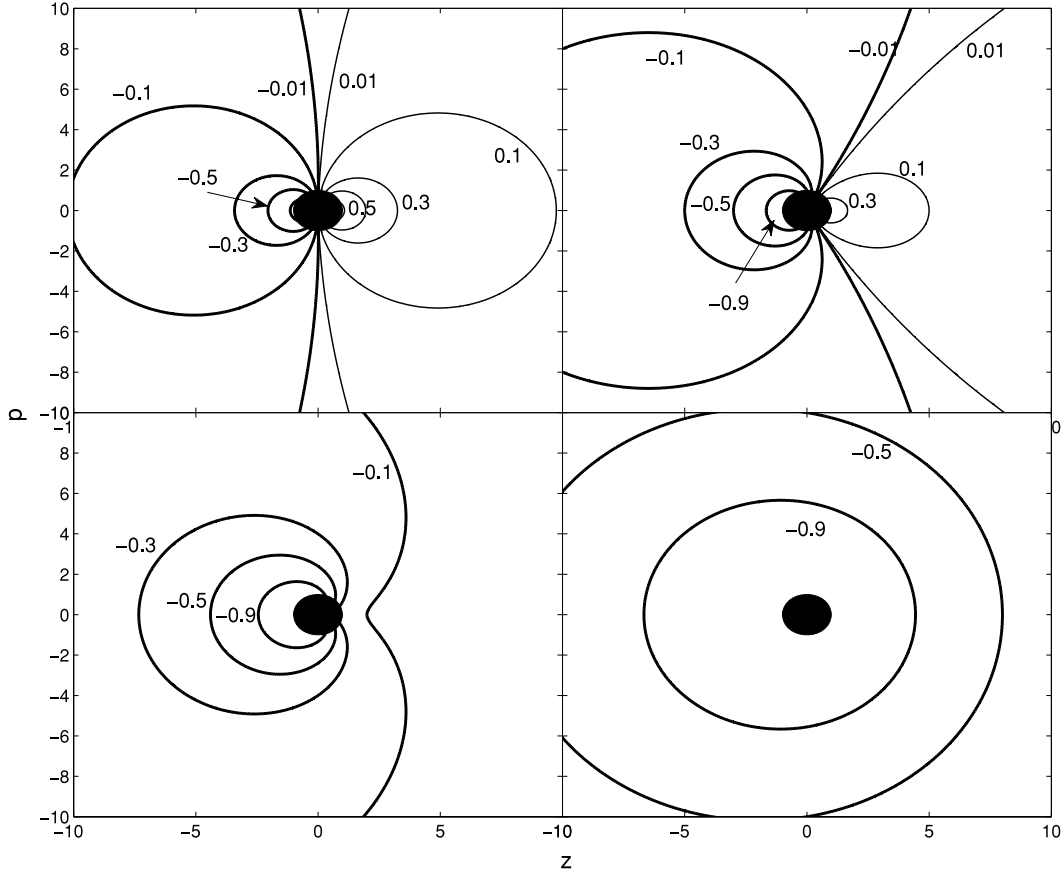


Figure 2. EFSs for the velocity law (24). The parameters are $g_0 = 2000$, $\beta_{\max} = 0.01$ (upper-left panel), $g_0 = 10$, $\beta_{\max} = 0.1$ (upper-right panel), $g_0 = 8.33$, $\beta_{\max} = 0.05$ (lower-left panel), $g_0 = 5$, $\beta_{\max} = 0.02$ (lower-right panel). Curves are marked by the parameter Λ , corresponding to the non-dimensional frequency at infinity. Curves: thick solid line – redshifted EFS; thin solid line – blueshifted EFS. The observer is located at $z \rightarrow \infty$.

Fig. 3 shows EFS for velocity laws (24) and (25) for $g_0 = 16$, $m = 2$. There are branches of both redshifted and blueshifted EFSs in front of the star, which makes possible the formation of both redshifted and blueshifted absorption lines (W-shaped profiles). From Fig. 3, we see that EFSs of the failed wind are not very different from those of the decelerated wind.

Each node in the $\{p_i\}$ grid marks a ray, and the problem of calculating the line profiles in p, z geometry is reduced to summation of contributions from all such possible rays. Each such ray is discretized, $\{z_k\}$, and we iterate from z_1 to z_2 looking for resonances and solving, if necessary, the non-linear equation (7).

When integrating over the EFS one encounters a specific numerical problem related to sudden jumps of the brightness occurring at such $p_i(v^\infty)$, at which the observer sees the boundary of the corresponding EFS(v^∞) (cf. Figs 2 and 3 and also Paper I for discussion). If not treated properly, there are spurious oscillations of the line profile observed for certain sets of parameters. To some extent, it may be cured by using finer discretization of the $\{p_i\}$ grid (see e.g. Marti & Noerdlinger 1977). We prefer a different approach: for each v^∞ , we numerically find such (z_j, p_j) at which $\partial p / \partial z = 0$ and then split the integral (23) into two parts:

$$\int_0^{p_j} I(v^\infty, p) p dp + \int_{p_j}^{p_{\text{out}}} I(v^\infty, p) p dp, \quad (28)$$

which also allows to have two $\{p_i\}$ subgrids each having different mesh density. The latter is important for those cases in which different branches of EFS are tightly packed near compact object. Thus,

we insure that p_j is always exactly on the boundary between cells and thus we eliminate spurious oscillations of the line profile.

6 LINE PROFILES

For the given set of parameters, g_0 , U^∞ , m , p and ϵ , we calculate line profiles from equation (23) adopting velocity laws (24) and (25) and the opacity law (26). All profiles are calculated assuming the size of the computational domain, $R_{\text{out}} = 50 R_c$. In case of the failed wind law (24), the value of initial velocity is fixed constant, $w_0 = 0.01$, and in all cases $v_{\text{th}} = 57 \text{ km s}^{-1}$.

6.1 Distorted P-Cygni and W-shaped profiles

Figs 4 and 5 show profiles for different g_0 , and velocity laws (24) and (25). From their corresponding upper-left panels, we infer that both decelerating and failed winds show P-Cygni profile provided the influence of the gravitational redshifting is negligible.

Note that if equation (25) is adopted the parameter U_0 does not equal the maximum velocity of the wind (see the discussion after equation 25). For example, Figs 4 and 5 are calculated for $U^\infty = U_0 = 156.4$, corresponding to $V^\infty = 0.03c$ in the case of Fig. 4, and $u_{\text{max}} = 112$, i.e. $u_{\text{max}} v_{\text{th}}/c = 0.02c$ in the case of Fig. 5. At large g_0 , the maximum blueshift, i.e. $y_{\text{max}}^+ = y^\infty = V^\infty = 156.4$, and the maximum projected velocity of the portion of the wind which is not obscured by the core determines the maximum observed redshifting: $y_{\text{max}}^- \simeq -67.6$. Hereafter, y^\pm is defined as a redshifted

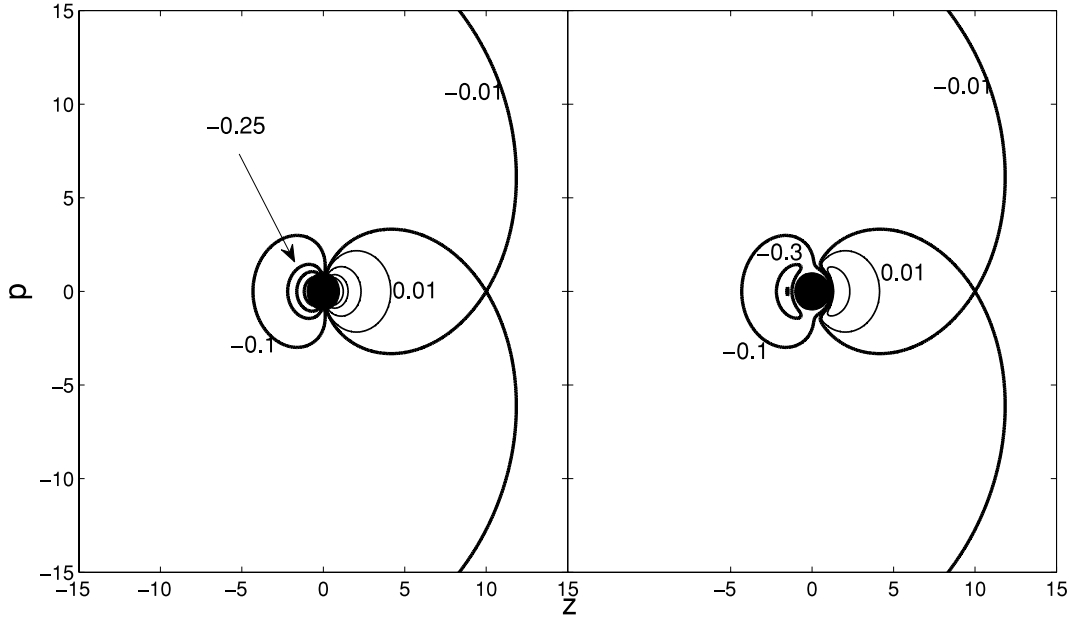


Figure 3. EFSs. Velocity laws (24, left-hand panel) and (25) with $\epsilon = 0.1$ (right-hand panel). Other parameters: $m = 2$, $g_0 = 16$, $\beta_{\max} = 0.15$. Thick solid line – redshifted EFS; thin solid line – blueshifted EFS.

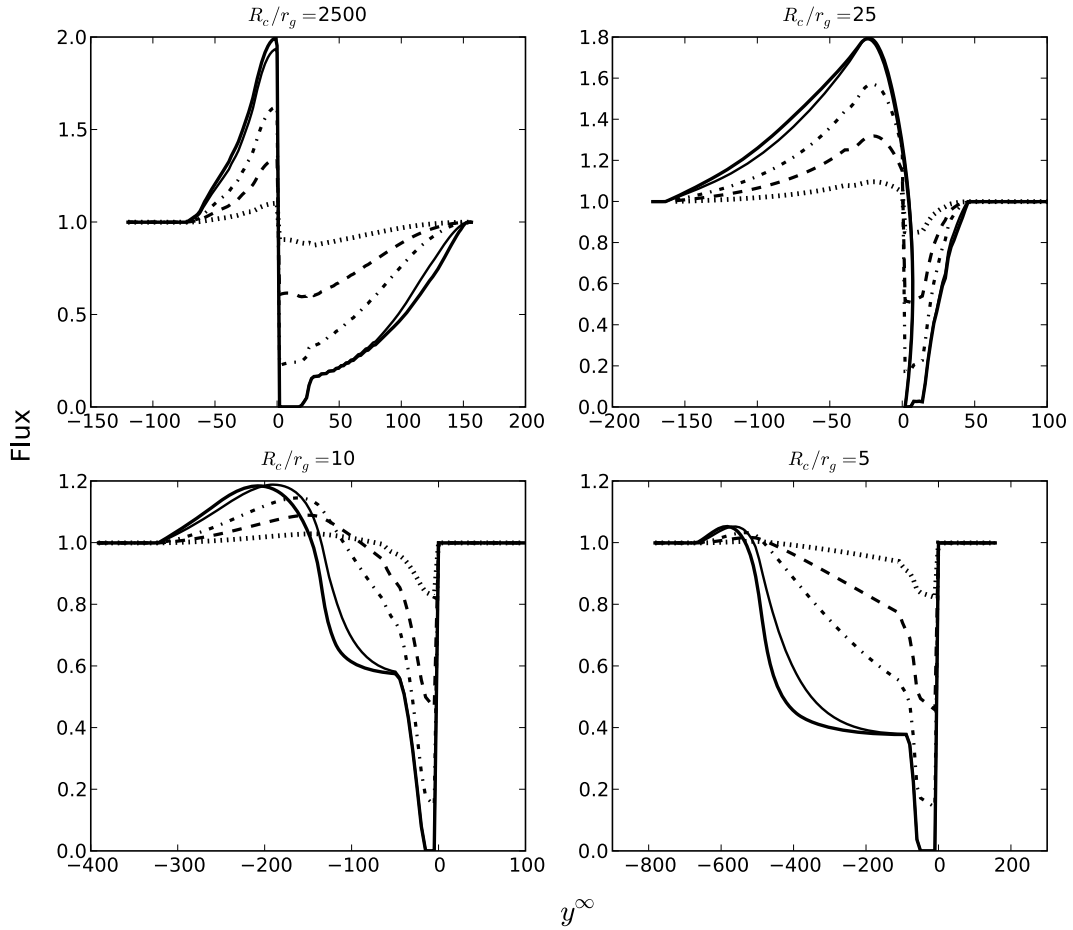


Figure 4. Line profiles for different launching radii. Optical depth law (26) with $k = 1$; velocity law (24) with $m = 1$. Curves: dotted – $T_0 = 0.1$; dashed – $T_0 = 0.4$; dot-dashed – $T_0 = 1$; solid (thin – $T_0 = 4$, thick – $T_0 = 10$). Other parameters: $U^\infty = 156.4$ corresponding to $V^\infty = 0.03 c$.

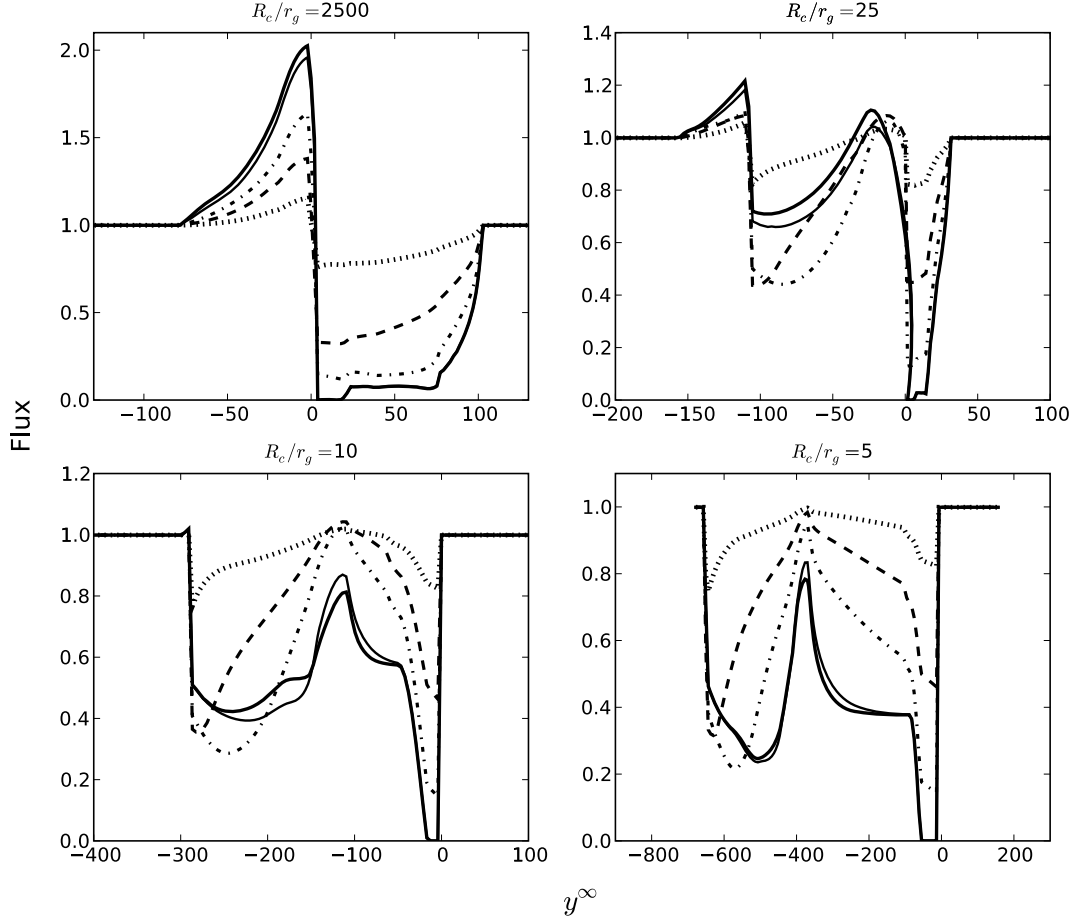


Figure 5. Line profiles from failed wind approximated by (25), with $m = 1$ and $\epsilon = 0.1$, $U_0 = 156.4$, which corresponds to $u_{\max} v_{\text{th}}/c = 0.02 c$, $u_{\max} = 112$ (see the text after 25 about the difference between U^∞ and u_{\max} , and U_0). Other parameters and the notation are the same as in Fig. 4.

or blueshifted non-dimensional frequency y^∞ . For the decelerating wind, u_{\max} is reached very close to the bottom of the wind, where gravity is strong, opposite to the case considered in Paper I, where maximum velocity is reached far from the star where gravitational redshifting is negligible.

The position of the redward edge of the line is determined from the approximate relation: $y_{\max}^+ \simeq u_{\max} - \zeta/(2g_0)$. For $g_0 = 25$, we have $y_{\max}^+ = 52$, and from upper right of Fig. 4 we infer $y_{\max}^+ \simeq 46$. Comparing to Fig. 4, we see that this approximate formula works well if u_{\max} is located close to the star.

The velocity law (24) generates the opacity distribution which has a maximum far from the star, while failed wind (25) leads to the opacity law, which peaks close to the photosphere (cf. Fig. 1). There are no W-shaped profiles in Fig. 4. If opacity peaks close to the photosphere, as in Fig. 5, then profiles with two absorption troughs separated by ‘emission’ component are observed.

From Fig. 5, we can assume that W-shaped profiles are more likely to be observed from the failed wind (25) rather than from the case of the decelerated wind (24).

To verify this assumption, we calculate profiles for the velocity law (24) adopting opacity distribution which peaks at the photosphere in case of the velocity law (24):

$$\tau_r(w) = T_0(k+1)w^k. \quad (29)$$

The results are shown in Fig. 6, where both sets of profiles are calculated for $g_0 = 10$.

We conclude that a short acceleration phase of the failed wind is critical for the formation of the W-shaped profiles.

One can note small spikes of intensity apparent in Fig. 6, they are most prominent in the absorption edge within the redshifted part of the profile (Fig. 5, upper-right panel). In Fig. 6 at the redshifted part of the spectrum they are observed for both of $V^\infty = 0.03 c$ (left-hand panel) and $V^\infty = 0.2 c$ (right-hand panel). The position of such a spike is independent of τ and can be understood adopting the following considerations: if gravitational shifting is negligible, a typical wind with $v \sim 1/r$ law has EFS which looks as two symmetrical loops in $p-z$ plane (for fixed $\pm y^\infty$) with respect of the $z = 0$ plane (i.e. as in Fig. 2, upper-left panel).

As g_0 decreases, the redshifted loop covers the star from the observer and at higher redshifts (lower g_0) the loop shifts further behind the star and covers only a fraction of it (Fig. 3, lower-left panel). This is due to the combination of the gravitational redshifting and strong Doppler redshifting and blueshifting at the photosphere. For lower g_0 (higher redshifts), EFS is obscuring less of a stellar disc, and such partial coverage results in interception of a lesser fraction of the direct flux of the core. Additional flux in the spike comes from the continuum radiation scattered by the same EFS.

The position of such spikes, y^- , is approximately determined by gravitational and transverse Doppler redshifts at the photosphere, $y^- \sim -\zeta/(2g_0) - \beta^2\zeta/2$, at $x = 1$; adopting parameters used to plot Fig. 6 (left-hand panel), we calculate $y^- \simeq -262$, while the figure gives $y^- = -291$.

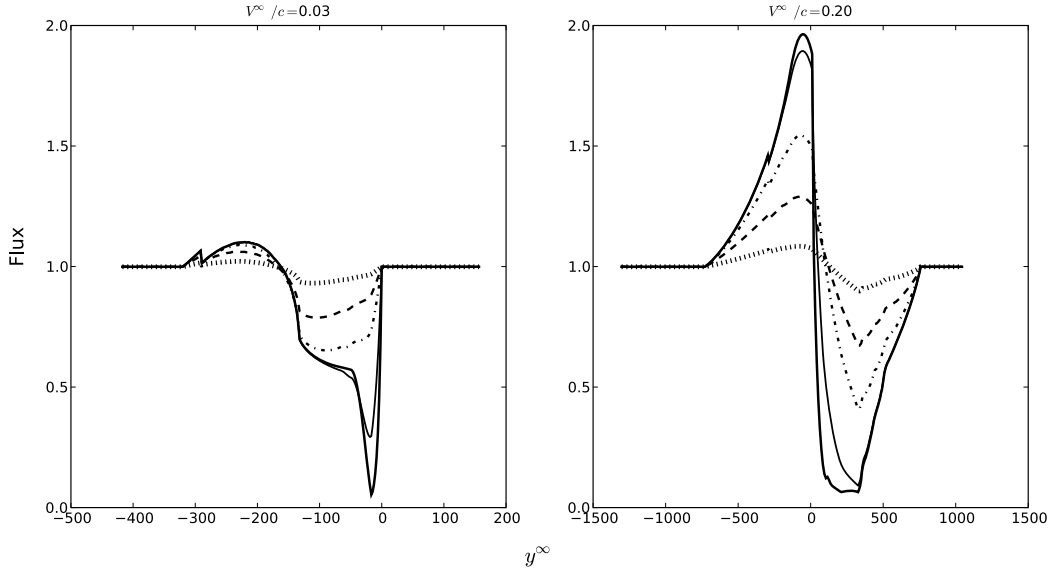


Figure 6. Line profiles from decelerated wind with the velocity law (24), with $m = 1$, and opacity law (29); both sets of profiles are calculated for $g_0 = 10$; $V^\infty = 0.03c$ (left-hand panel), $V^\infty = 0.2c$ (right-hand panel). Curves: dotted – $T_0 = 0.1$; dashed – $T_0 = 0.4$, dot-dashed – $T_0 = 1$; solid (thin – $T_0 = 4$, thick – $T_0 = 10$).

The velocity at $x \simeq 1$ is high and even a small deviation of μ from zero produces significant normal Doppler blueshifting or redshifting; the effect is larger at larger v , e.g. for the case of $V^\infty = 0.2c$ (Fig. 6, right-hand side) we have the predicted $y^- \simeq -364$ and the observed $y^- \simeq -286$, which is closer to the shift produced by the gravitational field alone, $y_{\text{grav}}^- \simeq -260$. From the above considerations, it is clear that position of such spikes is independent of the actual distribution of opacity.

6.2 Inverted P-Cygni profiles

Fig. 7 shows profiles from failed and decelerated wind. In the case of the decelerated wind, varying m in (24) or k in (26) results in the distortion of the P-Cygni profile. If the wind decelerates more rapidly (larger m) then the system of EFS is located closer to the star, and the lower surface area of EFS results in lower intensity of the profile (upper-left panel). The effect from increasing k in the opacity distribution is understood from Fig. 1, i.e. in the case of the velocity law (24) there is more opacity at the same radius x if k is larger, resulting in that both the local contribution, $S(1 - e^{-\tau})$, and the attenuation, $I_{\text{c}}e^{-\tau}$, is larger.

For the same setup of parameters shapes of profiles from the failed wind are completely different. From Fig. 7 (upper-right panel), we see that as m increases the P-Cygni profile first transforms to the W-shaped and then to the *inverted* P-Cygni.

To understand such behaviour, we note the W-shaped profiles are observed (at sufficiently strong gravity) only in special cases of the accelerated wind (see Paper I), being very sensitive to the distribution of the opacity.

In the case of accelerated wind in most cases, there is a redshifted EFS behind the star at large x , because only Doppler redshifting is important there. In result, the surface area of the corresponding redshifted EFS is larger and its emission overwhelms the redshifted absorption. In the case of the decelerated or failed wind, the maximum Doppler redshifting and blueshifting are made by the gas which is close to the star.

To produce an absorption line, the EFS should be in front of the star and needs to have surface area to cover enough of a star.

Roughly, the same-shape, low-surface-area EFS is situated behind of the star, and (i) if it has small surface area it reflects only a relatively small fraction of the flux towards the observer and (ii) because of the obscuration by the core the flux received by the observer is much lower.

Thus, sufficiently strong gravity ‘quenches’ the blueshifted EFS in front of the star and thus there is no blueshifted absorption but only a strongly redshifted one. On both sides of the star, the Doppler blueshift from the gas is comparable with gravitational redshift (e.g. roughly at $\mu \lesssim \pi/2$). This emission adds to the radiation of the core. In result, the emission is blueshifted with respect to the redshifted absorption trough as shown in Fig. 7 (upper-right panel). Understanding that in the decelerated wind case the gravitational redshifting is capable of producing inverted P-Cygni profiles is one of the major findings of this work.

It is instructive to investigate inverted P-Cygni profiles by changing the duration of the acceleration phase (i.e. ϵ in 25): the smaller ϵ the shorter is such phase (Fig. 1). In the case of the wind which is ‘almost’ purely decelerating, $\epsilon = 0.02$, the results are shown in Fig. 8 (left-hand panel).

Increasing m has the following consequences: the distortion of P-Cygni profile (dashed); the formation of W-profile (dotted, thin solid) and finally the transformation to the inverted P-Cygni profile. The latter is characterized by a relatively weak absorption line superimposed on the blueshifted emission (thick solid). In the case of $\epsilon = 0.2$, the behaviour is qualitatively the same: modified P-Cygni, W-shaped and inverted P-Cygni.

7 DISCUSSION

Studying the influence of the gravitational redshifting on the shape of spectral line profiles, we adopt two basic scenarios for the wind dynamics. In Paper I, we calculated profiles from monotonically accelerated winds (stellar-type winds and homologous expansion). It was established that gravitational redshifting is of significant importance, being able to modify and distorting line profiles considerably.

Profiles are sensitive not only to wind dynamics but also to the distribution of the opacity. Given the gravitational redshift is strong

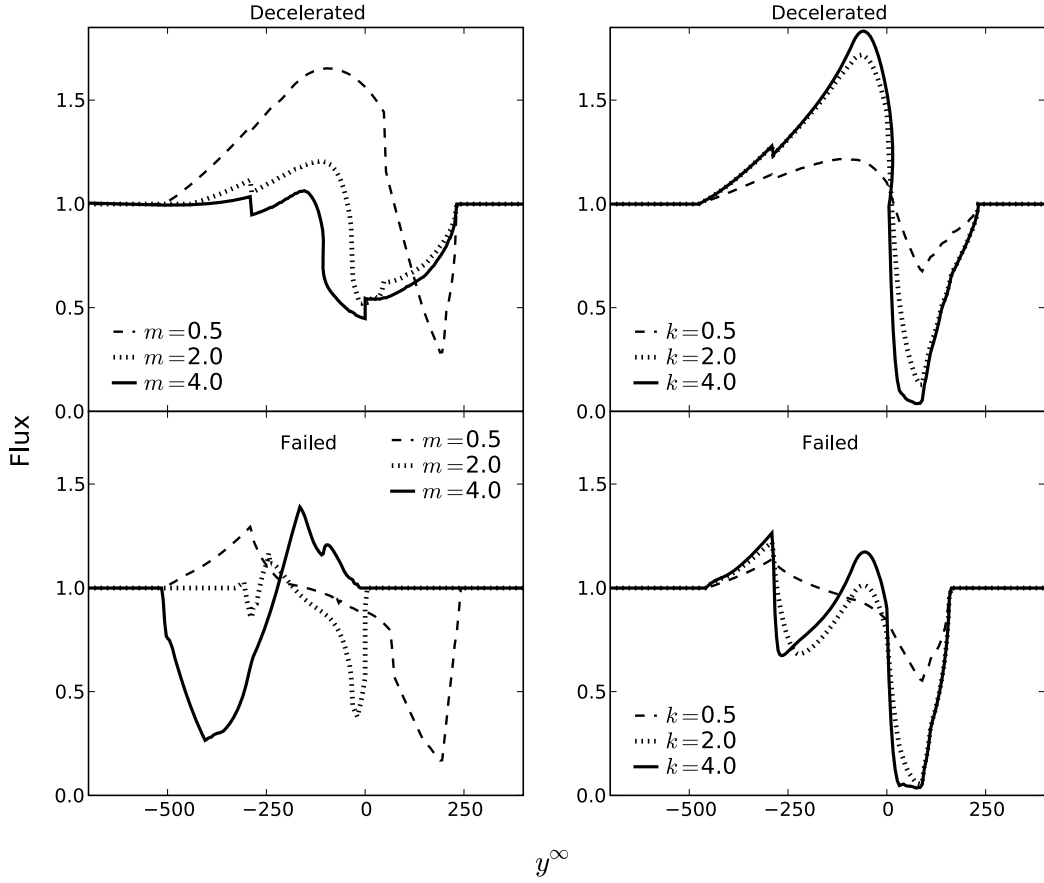


Figure 7. Line profiles for different velocity laws. Upper panels: curves for different m (i.e. slope of the velocity profile) in (24) and (25) and fixed $k = 1$ in (26). Bottom panels: different k (i.e. power index in the opacity law) in (26) and fixed $m = 1$ in (24) and (25). Other parameters: $g_0 = 10$, $V^\infty = 0.1 c$, $T_0 = 1$ and $\epsilon = 0.1$, if the velocity law (25) is adopted.

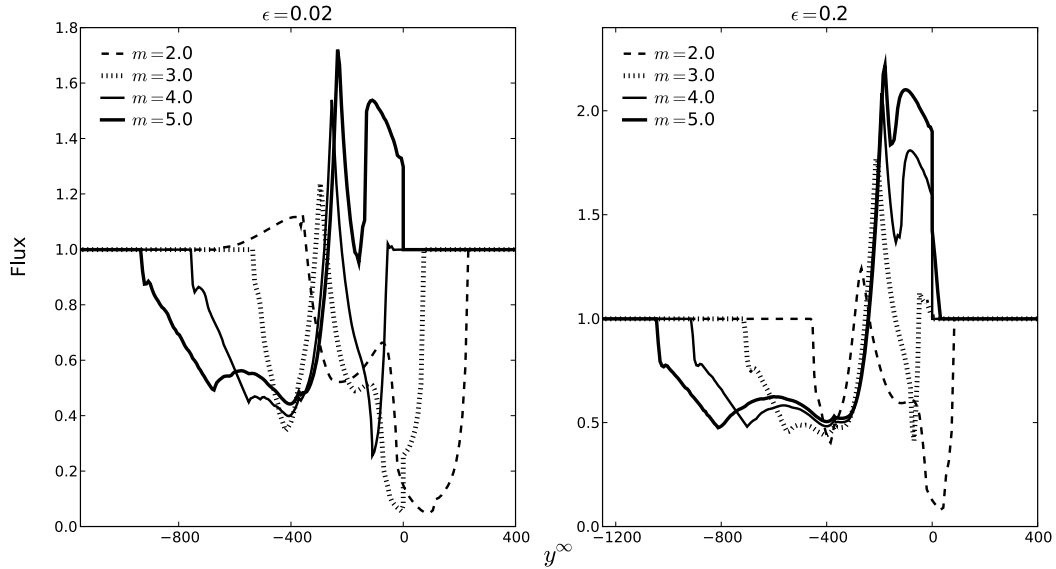


Figure 8. Line profiles from failed wind (29): left-hand panel – $\epsilon = 0.02$; right-hand panel – $\epsilon = 0.2$. Curves are for different values of m at (29). Other parameters: $g_0 = 8$, $V^\infty = 0.2 c$. Opacity law (26) with $k = 1$.

enough and the terminal velocity, V^∞ , is either much smaller than the escape velocity at the base of the wind or the distribution of the opacity strongly peaks close to the star, then a new type of profile, a W-shaped profile, is produced.

We can imagine a situation (X-ray bursters as an example) when energy is deposited into the wind during a short initial pulse, and after that time the wind is decelerating. In this paper, we consider winds which are either decelerating, according to $v(r) \sim 1/r^m$ law,

or ‘failed’, i.e. described by the bridging formula (25). In the latter case after a short accelerating phase, when $v(r) \sim (r - R_c)^m$, the wind velocity decreases according to $1/r^m$ law (cf. Fig. 1). In both cases, the wind reaches its maximum velocity V^∞ in the region where gravity is strong.

If there would be no absorption then the emission from the wind would be observed as a redshifted emission line having an approximately symmetric profile. In the case of the stellar-type wind $v(r) \sim (1 - R_c/r)^\alpha$ far from the compact object, Doppler blueshifting always overwhelms gravity and as a result there is always a possibility to have blueshifted absorption line. This absorption eats away blueward part of the emission line and produces a P-Cygni-type profile. On the other hand, inner parts of the wind also have velocities which are not large enough for the Doppler blueshifting to overwhelm gravitational redshifting, and such absorption eats away the redward part of the emission line. The result is that in certain cases these reshifted and blueshifted lines are combined together being separated by the emission component producing a W-shaped profile.

The case of the decelerated wind is different. Such a wind has its maximum velocity from the very beginning. The maximum Doppler blueshift is reached close to the photosphere, where sufficiently strong gravitational redshifting can overwhelm it. If there is an absorption, it will be redshifted, and so it is basically the regime where the photospheric line eats away the redward part of the emission from the wind. In such a case, the inverted P-Cygni profile is produced. Depending on how quickly the wind decelerates, there also may be an absorption occurring far from the star, i.e. eating away the blueward part of the line and producing a W-shaped profile similar to the case of the monotonically accelerated wind.

Three factors make inverted profiles possible: (i) strong gravity which competes with the Doppler effect; (ii) the maximum velocity of the wind is approached in the region where gravitational redshifting is strong enough to overwhelm it and (iii) at larger radii the wind quickly decelerates.

If the energy is deposited into the wind during a short initial pulse and the line is indeed formed in the vicinity of the compact object then it is likely to be transient, and profiles similar to those obtained in this paper should be considered as snapshots of different stages of expansion. The profile of a line from the early stage of expansion would be different from the profile of the same line at later times. Though we believe that obtained profiles are robust, the need of deducing physical conditions of the line-forming plasma in a real object would question simple approximations adopted in this paper, and such problem should be treated using methods of the full three-dimensional modelling (such as in Dorodnitsyn & Kallman 2009).

8 CONCLUSIONS

Several conclusion can be drawn about the influence of strong gravitational redshifting on profiles of spectral lines from failed and decelerated winds.

(i) At large R_c/r_g , where gravitational redshifting is negligible, decelerated winds (24) and failed winds (25) produce profiles with shapes similar to each other and to P-Cygni profile. Profiles from the failed wind have absorption troughs which are flatter than those from the decelerating wind.

(ii) If R_c is smaller than several tens of r_g , the effect of the gravitational shifting is significant. The strength of the effect depends on

the duration of the acceleration phase (parameter ϵ): profiles from decelerated wind ($\epsilon = 0$) are ‘equivalent’ to P-Cygni, i.e. they have absorption trough which is blueshifted with respect to the emission peak. Changing the slope of the velocity profile or changing the opacity distribution influences mostly the net intensity within the emission/absorption components; if $\epsilon > 0$ (failed wind) profiles are W-shaped, sometimes with additional weak emission component at the redward part of the profile (sawtoothed profile). Such profiles are obtained in many cases when R_c is less than approximately $20\text{--}30 r_g$. The effect of the gravity does not depend on V^∞ as sensitively as in the case of monotonically accelerated wind.

(iii) If failed wind is decelerating quickly (e.g. the parameter $m \gtrsim 3\text{--}4$ in (25) for $R_c = 10 r_g$, $V^\infty = 0.1 c$) the inverted P-Cygni profile is observed. Increasing the rate of the wind deceleration (i.e. m) first produces the distorted P-Cygni profile, then changes it to W-shaped and then at higher m produces the absorption–emission inverted P-Cygni profile.

ACKNOWLEDGMENTS

This research was supported by an appointment at the NASA Goddard Space Flight Center, administered by CRESST/UMD through a contract with NASA and by grants from the NASA Astrophysics Theory Program 05-ATP05-18.

REFERENCES

- Beals C. S., 1931, MNRAS, 91, 966
- Capri M. et al., 1970, preprint (astro-ph/0906.2438v1)
- Dadina M., Capri M., Malaguti G., Ponti G., de Rosa A., 2005, A&A, 442, 461
- Dorodnitsyn A., Kallman T., 2009, ApJ, 703, 1797
- Castor J. I., 1970, MNRAS, 149, 111
- Castor J. I., Lamers H. J. G. L. M., 1979, ApJ, 39, 481
- Cottam J., Paerels F., Mendez M., 2002, Nat, 420, 51
- Dorodnitsyn A. V., 2009, MNRAS, 393, 1433 (Paper I)
- Fabian A. C., Iwasawa K., Reynolds C. S., Yong A. J., 2000, ApJ, 112, 1145
- Hummer D. G., 1969, MNRAS, 145, 95
- Hutsemekers D., Surdej J., 1990, ApJ, 361, 367
- Grachev S. I., Grinin V. P., 1975, Astrophysics, 11, 20
- Kuan P., Kuhl L. V., 1975, ApJ, 199, 148
- Marti F., Noerdlinger P. D., 1977, ApJ, 215, 247
- Matt G., Porquet D., Bianchi S., Falocco S., Maiolino R., Reeves J. N., Zappacosta L., 2005, A&A, 435, 857
- Nandra K., George I. M., Mushotzky R. F., Turner T. J., Yaqoob T., 1999, ApJ, 523, 17
- Paczynski B., Wiita P. J., 1980, A&A, 88, 23
- Puls J., Owocki S. P., Fullerton A. W., 1993, A&A, 279, 457
- Rauch T., Suleimanov V., Werner K., 2008, A&A, 490, 1127
- Rybicki G. B., Hummer D. G., 1978, ApJ, 219, 654
- Rybicki G. B., Hummer D. G., 1983, ApJ, 274, 380
- Reeves J., Turner M., Pounds K., O’Brien P., Page K., 2001, in Inoue H., Kunieda H., eds, ASP Conf. Ser. Vol. 251, New Century of X-ray Astronomy. Astron. Soc. Pac., San Francisco, p. 120
- Reeves J., Pounds K., Uttley P., Kraemer S., Mushotzky R., Yaqoob T., George I. M., Turner T. J., 2005, ApJ, 633, L81
- Sobolev V. V., 1960, Moving Envelopes of Stars. Harvard Univ. Press, Cambridge
- Yaqoob T., Padmanabhan U., 2003, ApJ, 604, 63
- Yaqoob T., Serlemitsos P., 2005, ApJ, 623, 112

This paper has been typeset from a \LaTeX file prepared by the author.